



# Assessing the electrochemical performance of hierarchical nanostructured CuO@TiO<sub>2</sub> as an efficient bi-functional electrocatalyst

Ayesha Mujtaba<sup>1</sup> · Naveed Kausar Janjua<sup>1</sup> · Tariq Yasin<sup>2</sup> · Sana Sabahat<sup>3</sup>

Received: 23 November 2018 / Accepted: 20 October 2019 / Published online: 2 November 2019  
© Iranian Chemical Society 2019

## Abstract

Fabrication and attractive performance of CuO nanoparticles coated onto TiO<sub>2</sub> substrate (CuO@TiO<sub>2</sub>) as electrocatalysts for glucose and methanol electrooxidation are detailed in this article. These bi-functional electrocatalysts were prepared by impregnating (5–25 wt%) CuO nanoparticles onto nanosized TiO<sub>2</sub> substrate and were characterized for morphology and composition. Cyclic voltammetry and electrochemical impedance spectroscopy provided a detailed account of their electrochemical capacity. All samples in CuO@TiO<sub>2</sub> series were tested for probable electrocatalysis; however, 5CuO@TiO<sub>2</sub> possessed significantly improved electrocatalytic activity for methanol and glucose electrooxidation. This can be attributed to the better conductivity of the electrocatalyst showing that electrocatalytic activity is limited by the amount of CuO loading on CuO@TiO<sub>2</sub> electrocatalyst. The involvement of the Cu (II) to Cu (III) reversible redox couple was evident in the electrocatalytic oxidation. The sensitivity of 7.15  $\mu\text{A mM}^{-1} \text{cm}^{-2}$  and a detection limit of 235.0  $\mu\text{M}$  for glucose at a signal to noise ratio of 3 were obtained using 5CuO@TiO<sub>2</sub>-modified glassy carbon electrode.

**Keywords** CuO@TiO<sub>2</sub> nanopowders · Cyclic voltammetry · Electrochemical impedance spectroscopy · Electrooxidation

## Introduction

The development of electrocatalytic materials has traditionally relied on precious metal nanoparticles such as Pt, Au, Pd, Ir, Ru and Rh. The journey from single precious metal to non-single precious metals and subsequently, precious metal oxides persisted for almost three decades [1]. Development of electrocatalysts without precious metals started toward the end of 20th century and is growing ever since.

**Electronic supplementary material** The online version of this article (<https://doi.org/10.1007/s13738-019-01797-x>) contains supplementary material, which is available to authorized users.

✉ Ayesha Mujtaba  
ayesha.mujtaba@live.com

✉ Naveed Kausar Janjua  
nkkausarjanjua@yahoo.com; nkjanjua@qau.edu.pk

<sup>1</sup> Department of Chemistry, Quaid-i-Azam University, Islamabad 45320, Pakistan

<sup>2</sup> Department of Metallurgy and Materials Engineering, Pakistan Institute of Engineering and Applied Sciences PIEAS Nilore, Islamabad, Pakistan

<sup>3</sup> Department of Chemistry, COMSATS University, Park Road, Chak Shahzad, Islamabad 44000, Pakistan

The strategy lying behind this important adaptation from one type of electrocatalysts, made out of rather expensive, vulnerable to corrosion and limited in quantities precious metals, to the new types of compounds with promising but unrestricted possibilities was steadily recognized. The need for active, stable and cost-effective electrocatalysts encouraged concerted investigations, resulting in the development of multi-component non-precious metal catalysts as well as their metal oxide counterparts [2]. In recent years, an increasing number of researchers have explored the production of novel nanoscale mixed metal oxides, noble metal-doped metal oxides, metal oxide–CNTs nanocomposites, metal oxide-polymer composites and metal oxide coupled bio derivative components [3].

Metal oxide nanomaterials such as NiO, CuO, CeO<sub>2</sub>, ZnO, CoO, Fe<sub>2</sub>O<sub>3</sub>, Co<sub>3</sub>O<sub>4</sub>, TiO<sub>2</sub>, MgO and Al<sub>2</sub>O<sub>3</sub> as well as their mixed metal oxide counter parts represent a growing asset in many industries. With their heightened chemical, physical and electronic properties compared to their bulk counter parts, these versatile materials have been widely in many applications such as environmental remediation [4], medical technology [5], energy production [6], water treatment [7], catalytic processes [8], solar cells [9] and sensor applications [10–12] to name a few. Considering the

properties of metal oxides and combining the two certainly broadens their application potential. Previous studies have shown that CuO supported on TiO<sub>2</sub> nanocomposites find applications in the field of gas sensing [13], photocatalysis [14], as nanofiller for corrosion resistance [15] and for degradation of organic dyes [16]. Glucose electrooxidation based on Ti–Cu–O nanotubes [17], CuO/TiO<sub>2</sub> nanotube arrays electrodes [18] and CuO/TiO<sub>2</sub> electrode fabricated on FTO [19] is also reported. CuO supported on TiO<sub>2</sub> as ternary composite for methanol and ethanol electrooxidation is also available [20].

In previous works [11, 12], we have demonstrated that CuO loaded onto Al<sub>2</sub>O<sub>3</sub> and CeO<sub>2</sub> substrates can be highly efficient electrocatalysts for methanol and glucose in alkaline medium. Inspired by previous studies, in this work, we systematically and carefully synthesized a series of nano-sized CuO@TiO<sub>2</sub> materials for electrocatalysis. The strategy for current work was to investigate electrochemically active ratio of CuO and TiO<sub>2</sub> mixed metal oxide system and their applications in electrooxidation of two model analytes: methanol and glucose. Methanol and glucose find significant applications in fuel cell technology [21] and the development of next-generation sensing devices, respectively [22, 23].

## Experimental

### Materials and reagents

Titanium dioxide (TiO<sub>2</sub>), copper nitrate hexahydrate (Cu(NO<sub>3</sub>)<sub>3</sub>·6H<sub>2</sub>O), ammonia solution, D-glucose (C<sub>6</sub>H<sub>12</sub>O<sub>6</sub>), methanol, potassium hydroxide (KOH), sulfuric acid (H<sub>2</sub>SO<sub>4</sub>), potassium ferrocyanide trihydrate (K<sub>4</sub>[Fe(CN)<sub>6</sub>]·3H<sub>2</sub>O), potassium chloride (KCl), absolute ethanol, Nafion<sup>®</sup> and deionized water (18.2 MΩ cm) were used throughout the experiments. All the chemicals were purchased from Sigma-Aldrich and used as supplied without further purification.

### Preparation of 5-25CuO@TiO<sub>2</sub> nanopowders

As purchased, TiO<sub>2</sub> substrate was calcinated at 500 °C for 2 h in order to obtain a neat anatase phase. The calcined sample was subjected to Fourier-transform infrared spectroscopy (FTIR), X-ray diffraction (XRD), scanning electron microscopy (SEM), energy-dispersive X-ray (EDX) and Brunauer–Emmett–Teller (BET) surface area analysis before further use. Impregnation of CuO on the substrate was carried out by wt/wt% method using copper nitrate precursor. Five CuO loads: 5%, 10%, 15%, 20%, 25% were prepared in this regard. Impregnation was carried out on pre-calcined titania support using requisite volume of copper

nitrate hexahydrate solution. All the samples were soaked overnight, dried in oven for 1 h. and further calcinated at 500 °C for 2 h. The final catalyst powders were finely ground in the presence of acetone, dried and subjected to material characterization (FTIR, XRD, SEM and EDX) as well as electrochemical characterization (cyclic voltammetry (CV) and electrochemical impedance spectroscopy (EIS)).

### Preparation of CuO@TiO<sub>2</sub>-modified electrodes

Glassy carbon (GC) electrode was selected as a modification platform due to its broad potential window, low background current, rich surface chemistry, low economic cost and appropriateness for various sensing and detection applications [24]. Prior to the modification, GC electrode was polished to a mirror finish on a felt pad using alumina powder (0.3 μm) and was then rinsed thoroughly with deionized water. The electrode was ultrasonicated in deionized water for 1 min. in order to remove any loose alumina particles and was later dried at room temperature. For the modification purpose, the working surface of the clean GC electrode was wetted with 2 μL of pure ethanol and 0.1 mg of thoroughly ground catalyst sample was carefully dropped onto it, this was followed by drop casting 2 μL of 0.5% Nafion solution as a binder. The electrode was air dried for 30 min. The prepared modified GC/(5–25)CuO@TiO<sub>2</sub>/Nafion electrodes were used for acquiring electrochemical data. For each type of modified electrode, pre-conditioning steps were performed before each electrochemical measurement in respective potential windows in order to reduce background current and obtain a steady voltammogram.

### Apparatus

The structural characterization of catalyst powders was performed by X-ray diffraction (PANalytical X'PERT High Score's diffractometer with a Cu Kα radiation, operating in the range of 20°–70°). FTIR spectra of the catalyst samples were recorded on Nicolet 5PC (Nicolet Analytical Instrument, in the range of 4000–400 cm<sup>-1</sup>). Surface morphology of the samples was observed by scanning electron microscopy (SEM) (JEOL-JSM-6490A) equipped with energy-dispersive X-ray microanalysis (EDX) to determine the elemental composition of the nanopowders. BET surface area, pore volume and pore size distribution were determined using Micromeritics Analyzer (ASAP 2020 V3.01 E).

The electrochemical measurements (cyclic voltammetry and chronoamperometry) were carried out at room temperature using a conventional three-electrode assembly with modified glassy carbon (GC) serving as the working electrode (with 0.07 cm<sup>2</sup> surface area), Pt wire as a counter electrode and saturated calomel electrode (SCE with 3.0 M KCl) as the reference electrode. All solutions were prepared in

freshly deionized water, and 10 mL of supporting electrolyte was utilized for each electrochemical measurement. Prior to each measurement, the solutions were purged with Ar gas. Cyclic voltammograms and chronoamperograms were recorded on potentiostat interface 1000 by Gamry. Gamry interface 1000 was also used for electrochemical impedance spectroscopy (EIS) measurements at a dc bias of 0.25 V with a signal of 5 mV over the frequency range of 0.1–100 kHz.

## Results and discussion

### Physical Characterization of TiO<sub>2</sub> and 5-25CuO@TiO<sub>2</sub> nanopowders

Figure S1 (a) in supplementary section shows the FTIR spectrum of TiO<sub>2</sub> substrate. Broad absorption band in the range from 500 to 1000 cm<sup>-1</sup> is assigned to Ti–O vibrations [25]. Pure TiO<sub>2</sub> has a strong and broad band in the range of 400–1000 cm<sup>-1</sup> due to Ti–O stretching vibrational modes corresponding to the anatase phase [25]. Typical stretching vibrations of the Cu–O bond were observed in the FTIR spectra of all of the loaded catalysts at around 480–400 cm<sup>-1</sup> (highlighted in the inset of Fig. S1 (b), implying that CuO has been fully incorporated into TiO<sub>2</sub> matrix [26].

XRD pattern in Fig. 1a shows high crystallinity for TiO<sub>2</sub> substrate. Peaks appearing at  $2\theta=25.3^\circ, 36.9^\circ, 37.7^\circ, 38.5^\circ, 48.0^\circ, 53.8^\circ, 55.0^\circ, 62.6^\circ, 68.7^\circ, 70.2^\circ, 75.0^\circ, 76.0^\circ, 82.7^\circ$  correspond to the diffraction patterns of (101), (103), (004), (112), (200), (105), (211), (204), (116), (220), (215), (301) and (303), respectively, of pure anatase phase of titania, (JCPDS No.21-1272) [27]. The non-appearance of peaks at

27.4° and 30.8° also refers to the absence of both the rutile and brookite phases indicating that TiO<sub>2</sub> has not undergone phase transformation during the heating process [28].

The results of XRD analysis for 5-25CuO@TiO<sub>2</sub> nanopowders are depicted in Fig. 1b. It is quite notable that the XRD spectra of all the samples are dominated by diffraction peaks of TiO<sub>2</sub> nanoparticles, while the signature peaks for CuO appear at  $2\theta=35.4^\circ, 58.3^\circ$  and  $61.5^\circ$  [29]. These signals are of weak intensity and begin to show at the beginning of 5 wt% CuO loading; however, these signals gradually sharpen and their intensity increases with the loading of CuO from 5 to 25 wt%. As clearly shown in Fig. 1, only characteristic peaks of anatase TiO<sub>2</sub> and CuO crystal are observed. There are no other crystalline forms of copper oxide (i.e., Cu<sub>2</sub>O) or copper–titanium oxide (i.e., CuTiO<sub>3</sub>) present [30]; indicating that copper oxide exists as monoclinic CuO phase after the impregnation process in all the impregnated samples.

The SEM image showing the morphology of TiO<sub>2</sub> nanopowder is illustrated in Fig. 2a. It is inferred that TiO<sub>2</sub> nanoparticles are spherical in shape, small sized and with narrow size distribution, though particle agglomeration is also apparent to some extent. An SEM micrograph as a representative of CuO@TiO<sub>2</sub> hybrid series is depicted in Fig. 2c. The surface morphology of TiO<sub>2</sub> (Fig. 2c, d) hardly seems to be changed after loading 5 wt% CuO onto it. The catalyst is composed of a continuous network of spherical particles. Small voids and hollows are clearly visible within the catalyst surface.

Results of the EDX analysis for TiO<sub>2</sub> nanopowder as well as the entire series are provided in supplementary section (Fig. S2 and Table S1). These results correspond well with

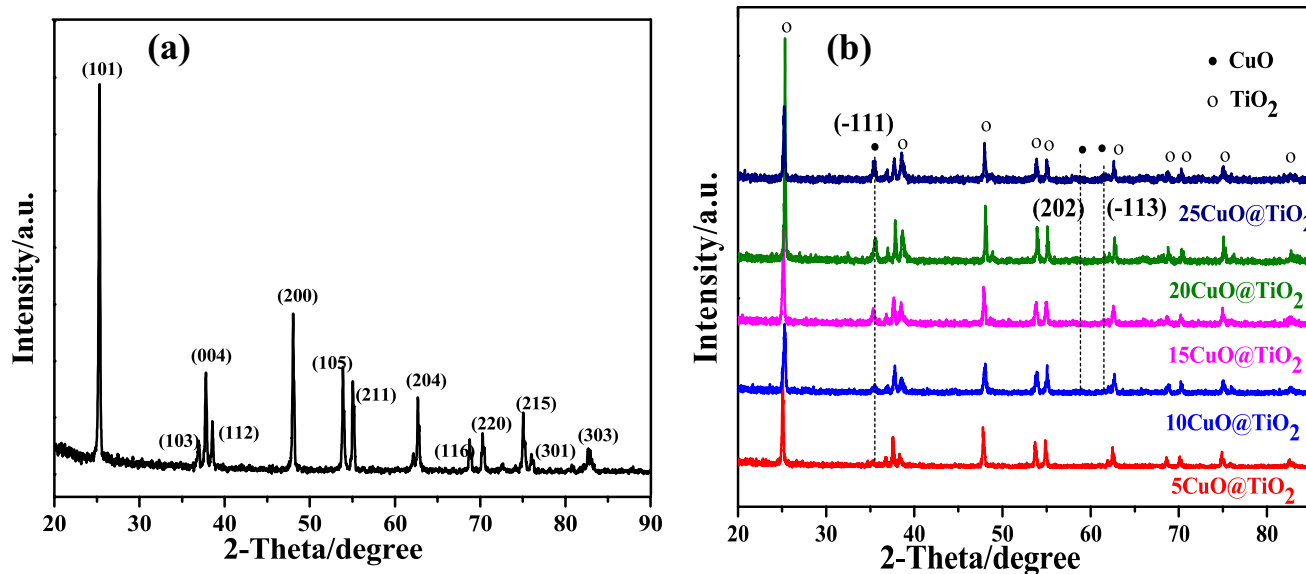
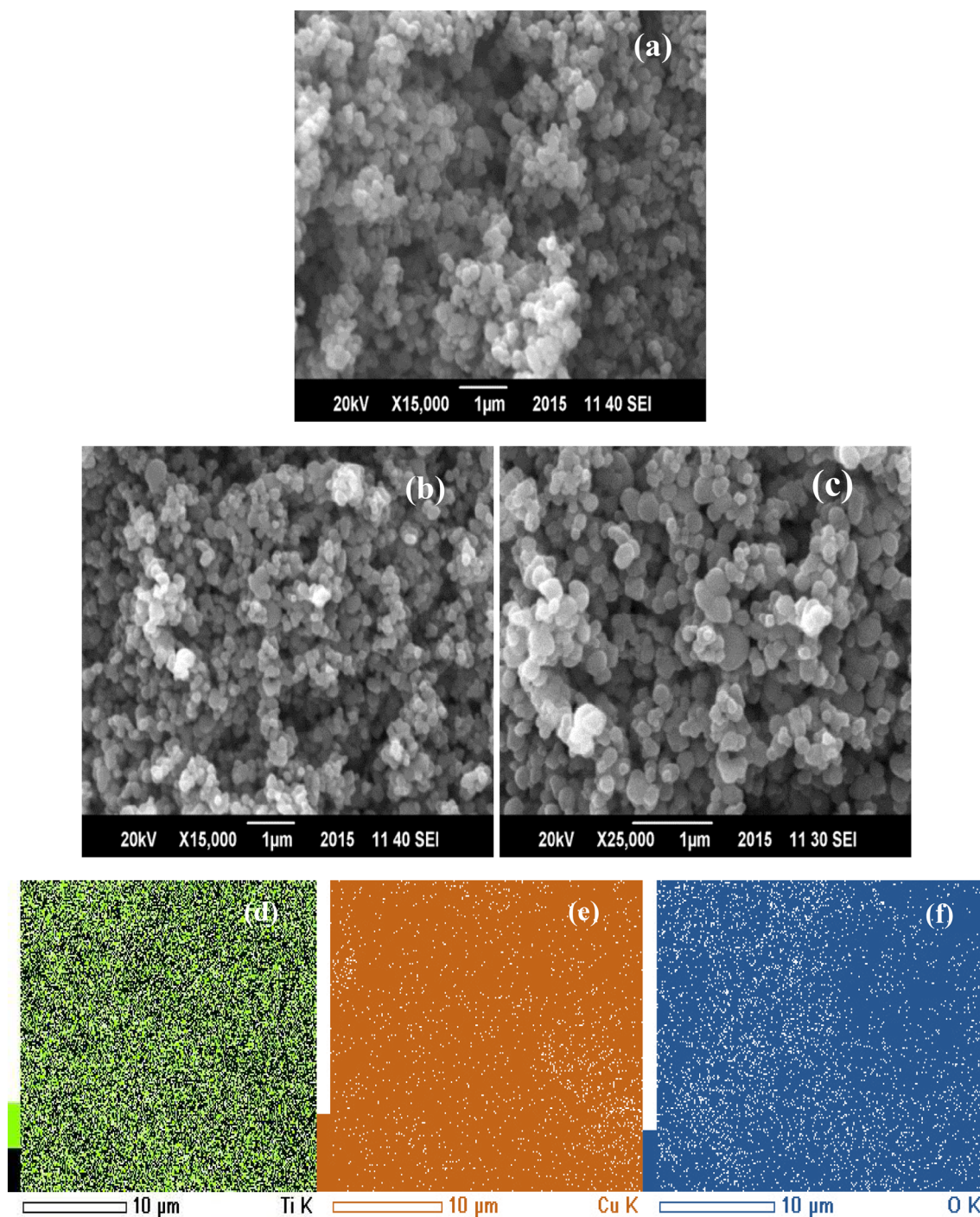


Fig. 1 XRD patterns of pure TiO<sub>2</sub> (a) and 5-25CuO@TiO<sub>2</sub> catalysts (b)



**Fig. 2** SEM micrograph of pure TiO<sub>2</sub> observed at 500 °C **a** SEM micrographs for 5CuO@TiO<sub>2</sub> nanopowders at different magnifications (**b**, **c**). EDX mapping of elemental distribution in 5CuO@TiO<sub>2</sub> catalyst (**d–f**)

the XRD results already discussed; where no additional peaks other than those of the components, TiO<sub>2</sub> and CuO could appear, hence indicating the purity of the catalyst samples. These data presented in Table S1 correspond to the stoichiometric loading of the catalyst and is in accordance with the theoretical loading of CuO onto TiO<sub>2</sub> substrate.

EDX mapping results depicted in Fig. 2d–f for the representative catalyst of this series revealed the homogeneous distribution of CuO onto TiO<sub>2</sub> matrix. This result complemented the SEM outcomes in Fig. 2b, c.

The surface area of the TiO<sub>2</sub> substrate sample was measured using the BET method. The N<sub>2</sub> adsorption–desorption

isotherms at 77 K and the pore size distribution evaluated by the Barrett–Joyner–Halenda (BJH) method are shown in Fig. 3a, b. The isotherm of  $\text{TiO}_2$  can be classified to be a type III isotherm with a type H3 hysteresis loop [31, 32] at the relative pressure,  $P/P_0$  of 0.7–0.9. The BET specific surface area was estimated to be  $8.21 \text{ m}^2 \text{ g}^{-1}$ , a total pore volume around  $0.17 \text{ cm}^3 \text{ g}^{-1}$  and the average pore width of  $546.3 \text{ \AA}$  was retrieved by BET.

### Electrochemical characterization

In order to provide further information on the properties of  $\text{TiO}_2$ -supported copper oxide catalysts, their electrochemical behavior was investigated via cyclic voltammetry in  $0.5 \text{ M H}_2\text{SO}_4$  solution (Fig. 4). It appeared that  $\text{CuO}$  was electrochemically reducible and oxidizable as embedded in  $\text{TiO}_2$  matrix. The electrooxidation and electroreduction of  $\text{CuO}$  occurred at about  $0\text{--}0.35 \text{ V}$  and  $-0.25\text{--}0.75 \text{ V}$ , respectively. However, there was a slightly noticeable shifting of both the anodic and cathodic peaks toward more positive and negative potentials, respectively, with an increase in  $\text{CuO}$  loading. This inference points toward some difficulty toward oxidation and reduction processes and may relate to the  $\text{CuO}$  particle agglomeration effect with increased  $\text{CuO}$  contents.

The electrochemical response of the electrodes modified with catalyst powders was in accordance with the EDX results and increasing the  $\text{CuO}$  content in respective samples resulted in an increase in the anodic and cathodic peak currents. Hence, there is a relationship between the observed peak currents and the amount of  $\text{CuO}$  that can be reduced and oxidized in respective catalysts [33].

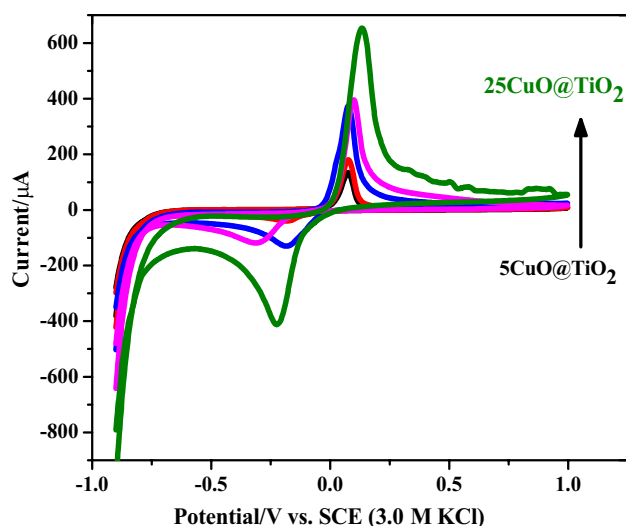


Fig. 4 Cyclic voltammograms for 5-25 $\text{CuO@TiO}_2$  nanopowders in  $0.5 \text{ M H}_2\text{SO}_4$

### Quantification of redox active $\text{CuO}$

The redox capabilities of  $\text{CuO}$  were demonstrated in acidic media by using cyclic voltammetry (Fig. 4). The electrochemistry of  $\text{CuO}$  was exploited to quantify the active amount of  $\text{CuO}$  present in the  $\text{CuO@TiO}_2$  catalyst powders on the surface of the electrode. By integrating the anodic peak, it is possible to obtain the charge value ( $q$ ) associated with the peak. From this value, the number of moles (mol.) of  $\text{CuO}$  actively involved in the redox reaction could be determined by the following equation [34]:

$$\text{mol.} = q/nF \quad (1)$$

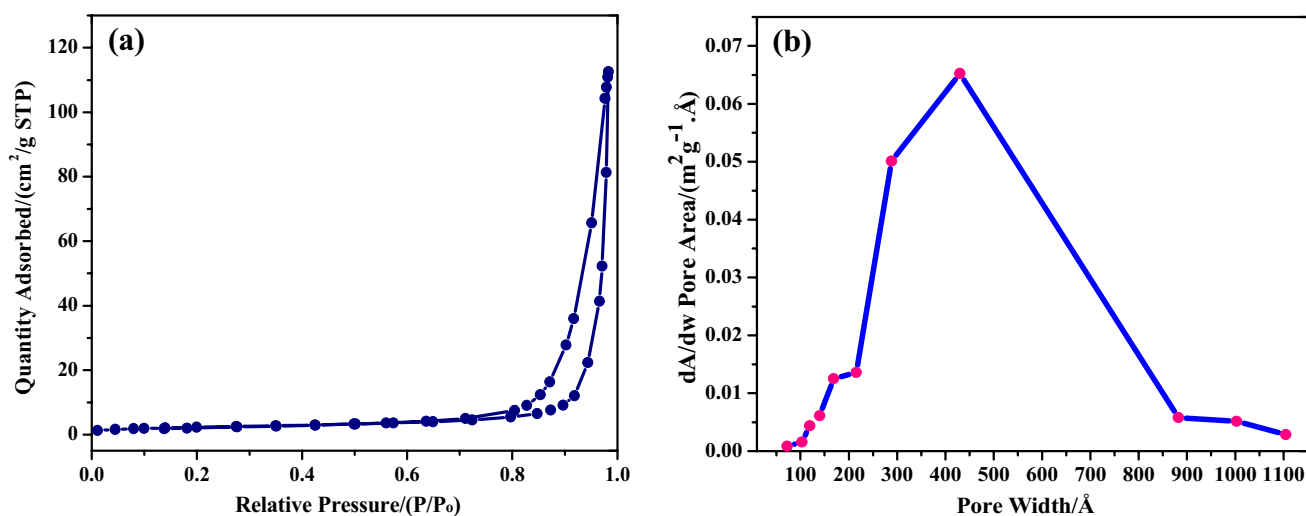


Fig. 3  $\text{N}_2$  adsorption–desorption isotherm for  $\text{TiO}_2$  substrate (a). Pore size distribution curve of  $\text{TiO}_2$  (b)

CuO surface concentration ( $\Gamma$ ), i.e., number of mol./cm<sup>2</sup> is calculated by equation:

$$\Gamma = q/nFA \quad (2)$$

where  $n$  is the number of electrons involved in the reaction (2 in this case),  $F$  is the Faraday constant (96,486 C mol.<sup>-1</sup>) and  $A$  is the geometrical surface area of glassy carbon electrode (0.07 cm<sup>2</sup>). By making use of Avogadro's number, we can also calculate the total number of molecules involved in the reaction. The derived electroactive amount of CuO is presented in Table S2.

### Heterogeneous electron-transfer dynamics in a redox probe: [Fe(CN)<sub>6</sub>]<sup>-4</sup>

Electron transport properties of the modified electrodes were studied in 3.0 M KCl solution containing 5.0 mM redox probe; potassium ferrocyanide. The electroactive surface area of 5-25CuO@TiO<sub>2</sub> electrodes was estimated by CV profiles using as a redox probe in 3.0 M KCl solution. Fig. S3 displays the CV results on the 5-25CuO@TiO<sub>2</sub>-modified electrodes. Well-defined reversible cyclic voltammograms were obtained for all the five sets of electrodes modified with catalyst powders. A noticeable variation in peak current was observed for all the five electrodes. The  $\Delta E_p$  values for 5-25CuO@TiO<sub>2</sub>-modified electrodes lied in the range of 0.062–0.108 mV, respectively. Electrode modified with 5CuO@TiO<sub>2</sub> showed the highest value of peak current while 25CuO@TiO<sub>2</sub> depicted the lowest one. Thus, 5CuO@TiO<sub>2</sub> catalyst sample indicated better conductive properties compared to rest of the samples in all series.

Randles–Sevcik equation [35] was applied to estimate the effective surface area of modified electrodes for K<sub>4</sub>[Fe(CN)<sub>6</sub>] probe at fixed experimental conditions, and the results are presented in Table S3. As predicted, the 5CuO@TiO<sub>2</sub> electrode possessed the highest effective surface area. The active surface area for the modified electrode followed the order: 5CuO@TiO<sub>2</sub> > 10CuO@TiO<sub>2</sub> > 15CuO@TiO<sub>2</sub> > 20CuO@TiO<sub>2</sub> > 25CuO@TiO<sub>2</sub>.

### Electrochemical impedance spectroscopy

EIS is an effective technique for probing the features of surface-modified electrodes; hence it was employed to provide noticeable insight into the electrochemical properties of 5-25CuO@TiO<sub>2</sub> catalytic materials. EIS was performed on all of the modified electrodes in 3.0 M KCl and 5.0 mM potassium ferrocyanide solution.

Two convenient ways of treating the impedance data are: the Nyquist plot which is the relationship of the imaginary resistance,  $Z''(\Omega)$ , and real resistance,  $Z'(\Omega)$ , components of the impedance, and the Bode plot in which absolute values of impedance or phase angle are plotted against the

frequency span. EIS study was conducted by analyzing both the Nyquist plot as well as the Bode plot for the modified electrodes [36] and Randles equivalent circuit model was proposed for the system under investigation, (inset in Fig. 5a) [37]. In order to develop a better understanding of the processes taking place at the electrode surface, the interpretation of these data was divided into two regions, the high-frequency and the low-frequency domains as indicated by the vertical line separation in Fig. 5.

The Nyquist plot Fig. 5a showed a significant difference in responses for all five electrodes. At high frequency, the intercept between the impedance part ( $Z''(\Omega)$ ) and the real impedance ( $Z'(\Omega)$ ), gives the magnitude of the solution resistance ( $R_s$ ) of the cell. The solution resistance offered by the cell is low and lies between 4 and 6  $\Omega$ . The other interesting feature of the high-frequency zone is the semi-circle observed for CuO@TiO<sub>2</sub>-modified electrodes. A semi-circle with a small diameter was observed for 5CuO@TiO<sub>2</sub> electrode. However, the diameter of the semicircle gradually expanded complying with the amount of CuO in successive samples. This small semicircle domain called the charge transfer resistance represents the electrode resistance and is closely related to the surface area and conductivity of the electrode material.  $R_{ct} = 0.3$  k $\Omega$  for 5CuO@TiO<sub>2</sub>, infers a very low electron-transfer resistance and good conductivity toward the redox probe. This electrode also depicted a much higher active surface area compared to rest of the samples as discussed in the earlier section. However, further enriching TiO<sub>2</sub> substrate with CuO did not prove to be effective and enhanced the electron-transfer resistance and a gradual drop was observed in rest of the higher loaded catalysts. Thus, the  $R_{ct}$  values varied in the order: 5CuO@TiO<sub>2</sub> > 10CuO@TiO<sub>2</sub> > 15CuO@TiO<sub>2</sub> > 20CuO@TiO<sub>2</sub> > 25CuO@TiO<sub>2</sub> with 5CuO@TiO<sub>2</sub> being a better electron-transfer facilitator.

At the low-frequency region, the 45° slope of the straight line of the Nyquist plots corresponds to the Warburg resistance ( $R_w$ ), which results from diffusion of ions in the electrolyte. The effect of the Warburg impedance and its contribution can be observed at the low-frequency region because the mass transport of the electroactive species may be limiting the electron-transfer process.

The EIS 300 nonlinear least squares curve fitting tool was used to fit equivalent circuit model to impedance spectra. Table 1 highlights in detail the results of the extracted data from equivalent circuit modeling as well as calculated apparent rate constant [38]. The higher  $k_{app}$  value for the 5CuO@TiO<sub>2</sub>-modified electrode is also an indicative of faster electron-transfer process at this electrode compared to the four other electrodes with higher CuO loadings.

Similar information is obtained by examining the Bode diagram, Fig. 5b, c.  $R_s$  and ( $R_s + R_{ct}$ ) are obtained straightforwardly from the  $Z''(\Omega)$  versus log frequency (Hz) plot, Fig. 5b, at high and low frequencies, respectively, using

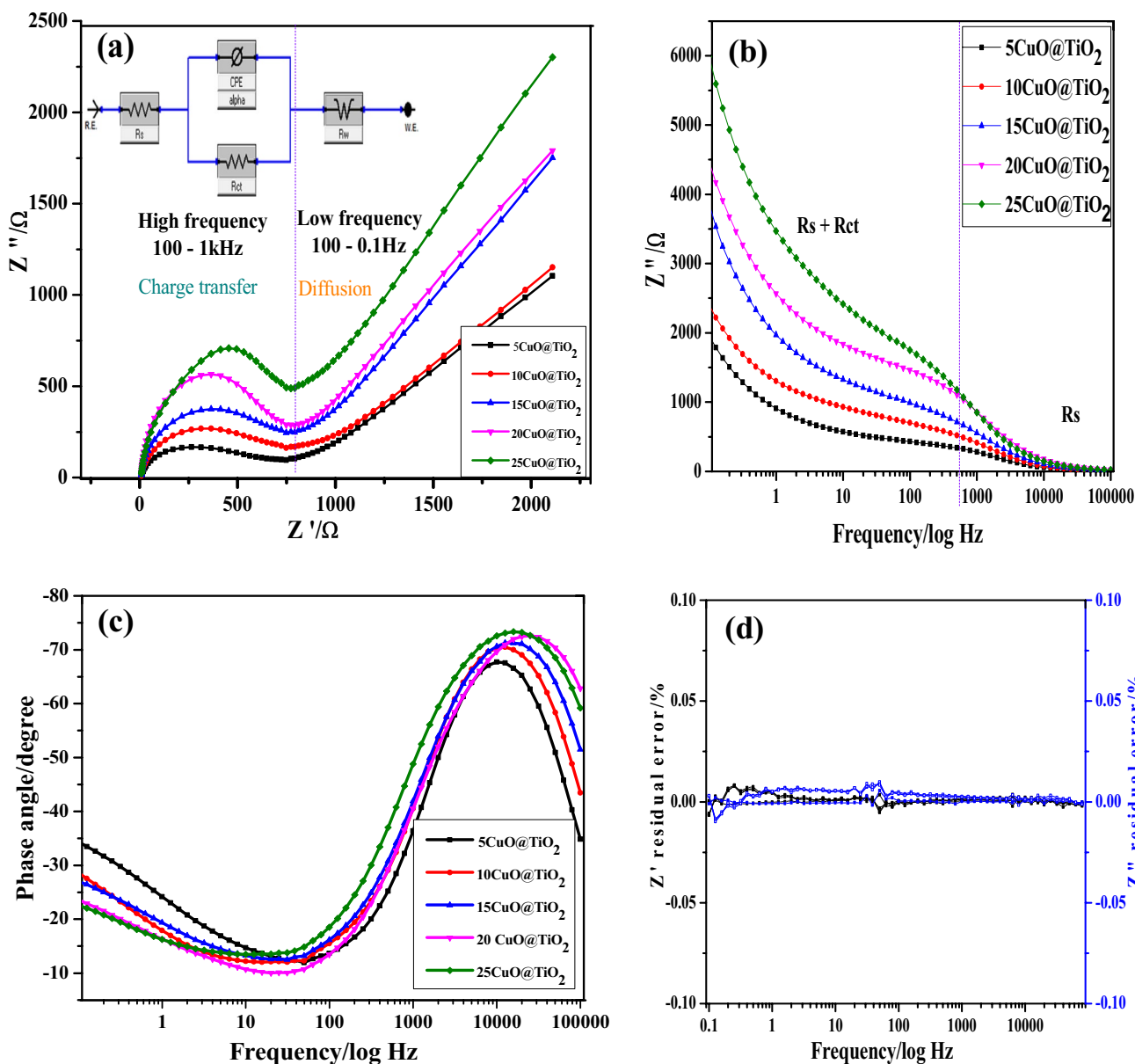


**Fig. 5** Nyquist plots for EIS measurements (a). At upper left corner of (a) is the equivalent circuit used for data fitting. Bode plots (logarithmic plot of frequency vs. impedance) (b) and logarithmic plot of

frequency vs. phase angle (c) at 5-25CuO@TiO<sub>2</sub>-modified electrodes. Kronig-Kramers transformation test (plot of log of frequency vs. error in  $Z''$  and  $Z'$ ) (d)

**Table 1** Parameters obtained by simulating the EIS data along with the calculated apparent electron-transfer rate constant,  $k_{app}$

Catalyst	$R_s$ ( $\Omega$ )	$R_{ct}$ ( $k\Omega$ )	CPE/F	$n$	$R_w$ ( $\Omega$ )	$k_{app}$ ( $cm\ s^{-1} \times 10^{-5}$ )
5CuO@TiO <sub>2</sub>	4.01	0.30	$9.8 \times 10^{-7}$	0.88	620	17.7
10CuO@TiO <sub>2</sub>	5.23	0.51	$2.5 \times 10^{-6}$	0.85	950	10.4
15CuO@TiO <sub>2</sub>	4.50	0.65	$5.5 \times 10^{-7}$	0.87	1400	8.18
20CuO@TiO <sub>2</sub>	4.23	1.00	$1.5 \times 10^{-5}$	0.86	2400	5.32
25CuO@TiO <sub>2</sub>	6.15	1.25	$5.0 \times 10^{-7}$	0.86	1800	4.25

the same argument as the Nyquist plot. The high-frequency region yielded a slope of close to zero, characteristic of a pure resistor, while the low-frequency region yielded a slope of  $< 1.0$  characteristic of a pseudo capacitor. In general, this data clearly suggest that the impedance of these electrodes varied from that of a pure resistor at high frequency to pseudo capacitor at the low-frequency region.

A purely capacitive element ( $C_{dl}$ ) was therefore replaced by a constant phase element (CPE) in the electrical equivalent circuit to obtain a good fit. CPE is the constant phase element which denotes the deviation from the ideal capacitance owing to the sample surface inhomogeneity. CPE comprises sub-element  $Q$  which relates to surface electroactive properties and  $n$  which arises from the slope of  $Z''$  vs.  $\log f$ . The value of  $n$  varies between  $-1$  and  $1$ . When  $n=0$ , the CPE represents a pure resistor; at  $n=1$ , a pure capacitor and an inductor at  $n=-1$ . At  $n=0.5$ , the CPE corresponds to Warburg impedance ( $R_w$ ). The presence of the CPE also indicates the porous nature of the electrode. An attempt to replace the ideal  $C_{dl}$  (double layer capacitance) with a CPE (constant phase element) in the modeling circuit proved successful in this regard. The  $n$  values provided in Table 1 are indicative of this pseudo-capacitive behavior.

From the Bode plots of phase angle vs.  $\log(f/\text{Hz})$  for the electrodes, all the electrodes presented a phase angle greater than  $60$  but less than  $90$  (which is expected for ideal capacitive behavior) indicating pseudo-capacitive behavior of the electrodes [39].

Finally, the Kronig–Kramers transformation test [40] was carried out on 5-25CuO@TiO<sub>2</sub> electrodes to examine the validity of the impedance data (Fig. 5d). The Kronig–Kramers transformation gave a  $\chi^2$  (Chi square) of  $2.11 \times 10^{-6}$  for 5CuO@TiO<sub>2</sub>,  $7.24 \times 10^{-6}$  for 10CuO@TiO<sub>2</sub>,  $27.84 \times 10^{-6}$  for 15CuO@TiO<sub>2</sub>,  $23.89 \times 10^{-6}$  for 20CuO@TiO<sub>2</sub> and  $24.72 \times 10^{-6}$  for 25CuO@TiO<sub>2</sub>. Therefore, the system satisfied all the conditions for very good impedance data (i.e., linearity, causality, stability and finiteness of the system). Thus, the test implied that the impedance data were validated with respect to impedances over a wide frequency range and were of very good quality.

## Application studies on CuO@TiO<sub>2</sub>-modified electrodes

### Electrocatalytic oxidation of methanol at CuO@TiO<sub>2</sub>-modified electrode

The electro activity of 5-25CuO@TiO<sub>2</sub> electrodes for methanol oxidation was studied by cyclic voltammetry using  $1.0 \text{ M}$  methanol solution in  $0.1 \text{ M}$  KOH. Cyclic voltammograms (CV) were retrieved during scanning between  $0.2$  and  $1.0 \text{ V}$  vs. SCE at room temperature. Comparative CV responses

for methanol oxidation on the working electrode modified with 5-25CuO@TiO<sub>2</sub> nanopowders are shown in Fig. S4. The 5CuO@TiO<sub>2</sub> composition mediated a better peak profile compared to rest of the powders. The catalytic behavior of this sample is expected on the basis of the EC/ET (electrochemical/electron transfer) properties rendered by this optimal material as discussed earlier. For the better conduction phenomenon in the optimal composition, 5CuO@TiO<sub>2</sub> can also be employed in fuel cell applications. A detection limit of  $1.27 \mu\text{M}$  for methanol electrooxidation at 5CuO@TiO<sub>2</sub>-modified electrode was also obtained from the CV data.

The effect of scan rate on oxidation peak current has been investigated in the range of  $10 - 500 \text{ mV s}^{-1}$ , Fig. 6a. The linear increase in the oxidation peak current with the square root of scan rate (Fig. 6b) is indicative of facile electron-transfer process at the electrode surface, clearly pointing toward electrocatalytic ability of the active material. Figure 6c and d presents variation in the oxidation peak current as a function of square root of the scan rates. These trends again are the indicative of the diffusion limited process at low scan rates. It suggests that the overall electrooxidation of methanol at the modified electrode is governed by diffusion of methanol to the surface redox sites which becomes kinetically controlled in the region of higher scan rates [41].

The diffusion character of methanol electrooxidation at lower scan rates was also confirmed by the linear dependence of  $\ln i_{pa}$  on  $\ln \nu$ . The electrocatalytic ( $EC_{cat}$ ) nature of the process was shown by the dependence of current function ( $i_{pa}/\nu^{1/2}$ ) on scan rate ( $\nu$ ) and this function varied exponentially with the scan rate in this study, [42]. A negative slope indicated that methanol electrooxidation is mediated in the presence of 5CuO@TiO<sub>2</sub> (Fig. S5).

### Glucose oxidation on CuO@TiO<sub>2</sub> electrodes

To demonstrate the functional potential of 5-25CuO@TiO<sub>2</sub> materials in the construction of biosensors, the electrochemical oxidation of glucose was carried out on the GC electrode modified with these nanopowders (refer to supplementary data for voltammetric responses of 10-25CuO@TiO<sub>2</sub> electrodes (Fig. S6 (f–i))). The measurements were performed in  $0.1 \text{ M}$  KOH solution with the gradual addition of glucose. Although all the electrodes had the ability to electrooxidize glucose at their surface; however, 5CuO@TiO<sub>2</sub> offered a better riposte (Fig. 7e). The increase in the oxidation peak current with glucose concentration from  $2.0$  to  $20.0 \text{ mM}$  is a manifestation of the catalysis (currents were recorded at a potential of  $+0.65 \text{ V}$ ). The prominent response of 5CuO@TiO<sub>2</sub> electrode toward the glucose oxidation may be ascribed to the higher surface area and enhanced electron-transfer capability compared to the other samples in this series.  $20.0 \text{ mM}$  glucose was the threshold concentration and the anodic current ceased to increase after that which may



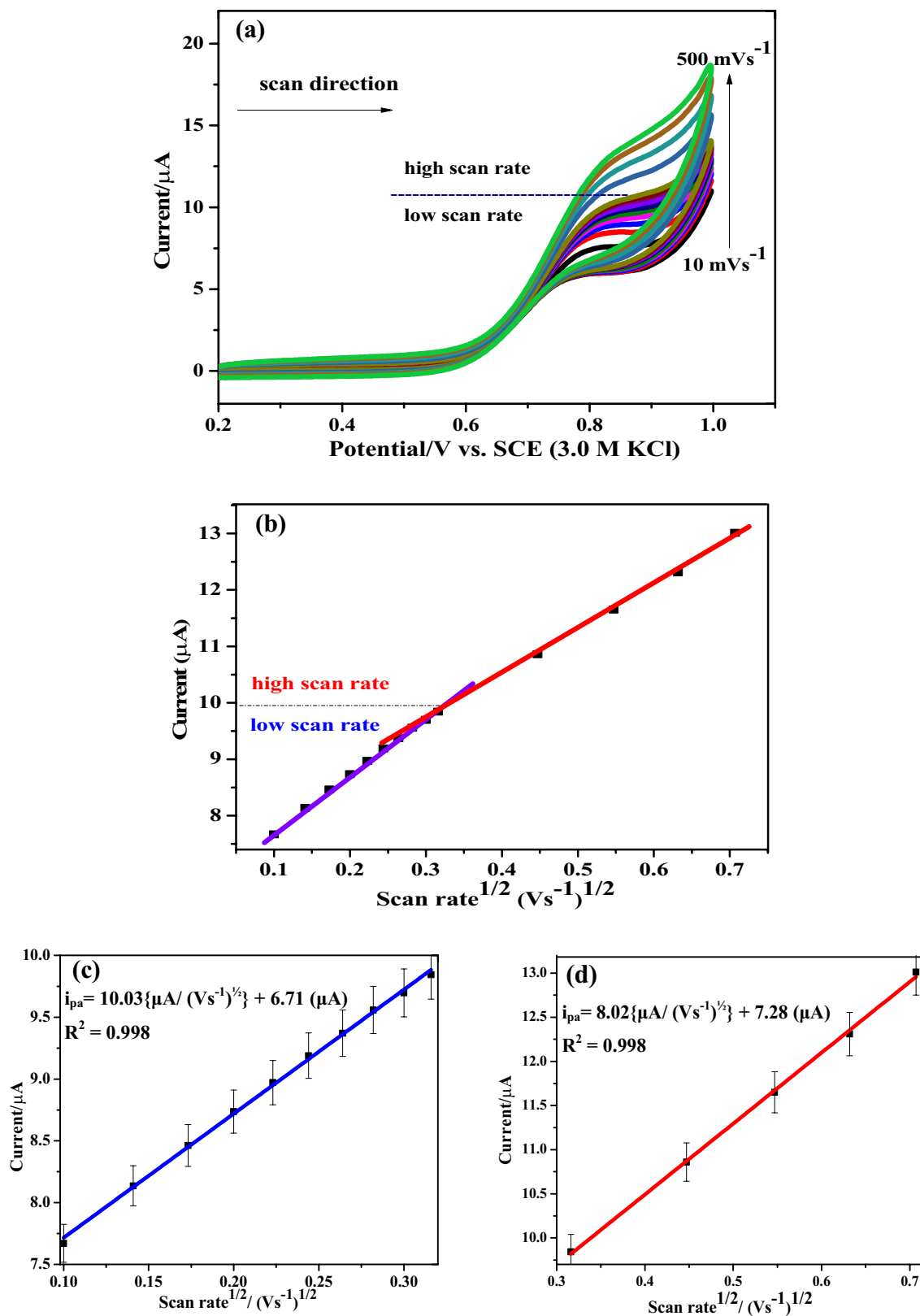


**Fig. 6** Cyclic voltammograms of 1.0 M methanol at 5CuO@TiO<sub>2</sub> electrode in 0.1 M KOH at scan range 10–500  $\text{mV s}^{-1}$  (a). Dependence of anodic peak current ( $i_{pa}$ ) on the square root of scan rate ( $\nu^{1/2}$ ) (b). Linear fitting for lower (c) and higher (d) scan rate ranges

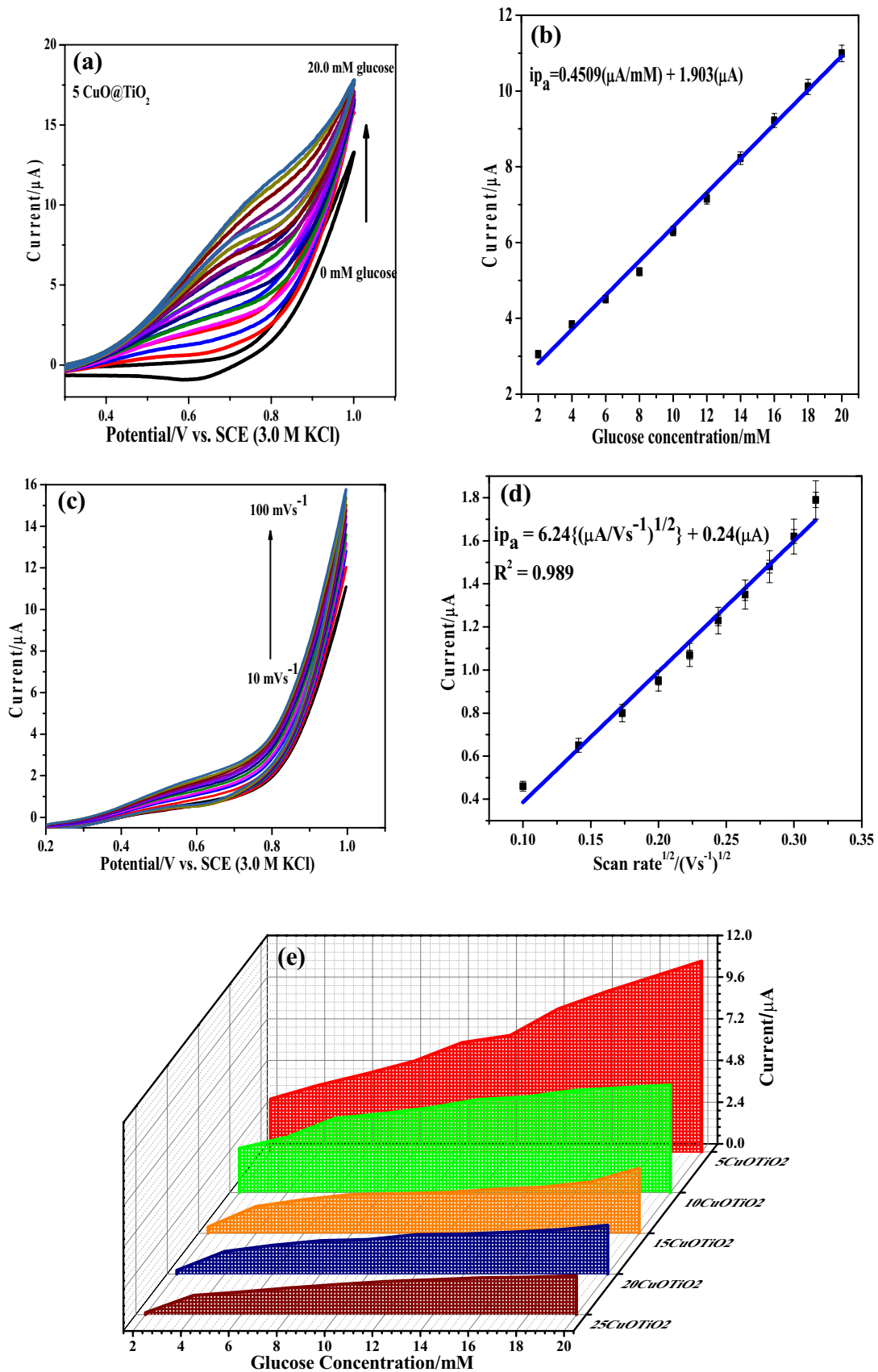


**Fig. 7** Electrochemical catalytic oxidation of glucose on 5CuO@TiO<sub>2</sub>-modified electrodes (a). Calibration plot of glucose concentration versus anodic peak current (b). Scan rate effect for 5CuO@TiO<sub>2</sub> electrode in 2.0 mM glucose and 0.1 M KOH (c). Linear fit regression plot for scan rate effect (d). 3D chart highlighting the anodic current trends for all the modified electrodes from 2.0 to 20.0 mM glucose concentration (e)

be attributed to passivation/blockage of electrode reactive sites or formation of glucose isomers which could block the catalytic sites [43]. From Fig. 7b, a linear fit equation was obtained and catalyst parameters relating to sensitivity were evaluated.

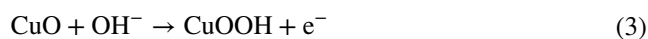
A sensitivity of 7.15  $\mu\text{A mM}^{-1} \text{cm}^{-2}$  and a detection limit of 235.0  $\mu\text{M}$  for glucose at a signal to noise ratio of 3 was obtained using 5CuO@TiO<sub>2</sub>-modified electrode. Table 2 highlights the comparison of upper and lower detection limits for 5CuO@TiO<sub>2</sub>-modified GC electrode with some of the similar electrode materials used for similar detection. A wide linear upper range of detection was recorded for the 5CuO@TiO<sub>2</sub> electrode.

The nature of glucose redox process was investigated by varying scan rate and observing the resultant oxidation current by cyclic voltammetry in 0.1 M KOH solution containing 2.0 mM glucose. A linear relationship of oxidation peak current (corresponding to a potential of +0.65 V) with the square root of scan rate (Fig. 7d) was observed.

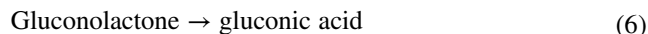
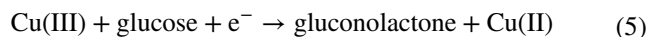
This linear relation is an indicative of diffusion controlled reaction and suggests that the overall oxidation of glucose at 5CuO@TiO<sub>2</sub>-modified electrode is controlled by diffusion of glucose to the surface redox sites [44]. The cyclic voltammograms on the modified electrode in glucose solution exhibited no characteristic peak during the cathodic scan, thereby showing that electron-transfer process to be completely irreversible.

### Mechanism of glucose electrooxidation on CuO@TiO<sub>2</sub>-modified electrode

The mechanism for glucose electrooxidation on CuO is widely agreed to be attributed to the conversion of Cu (II) to Cu (III) species in alkaline media [48]. The equation below describes the conversion of Cu (II) to Cu (III) specie and subsequently its involvement in the glucose electrooxidation.



or



We were able to detect and capture the subtle progression of Cu (II) to the electroactive Cu (III) specie via cyclic voltammetry. The cyclic voltammogram provided in Fig. 8a presents the species generated as the potential was scanned between -1.5 and 1.0 V in alkaline media [49]. It is pertinent to mention that Cu (III) specie is generated at a potential around 0.5 V and the onset potential for glucose electrooxidation at CuO@TiO<sub>2</sub>-modified electrodes is also in the same range; hence there is a direct participation of Cu (III) specie in glucose electrooxidation at CuO@TiO<sub>2</sub>-modified electrodes.

### Chronoamperometry

Chronoamperometry was employed as an effective technique to inquire not only about the electrochemical stability of prepared 5-25CuO@TiO<sub>2</sub>-modified electrodes in 0.1 M KOH + 2.0 mM glucose solution at room temperature, but also about the nature of the electrochemical process occurring at the electrode/electrolyte interface [50]. Fig. 9 presents the chronoamperometric curves for all the five modified electrodes traced for a period of 120 s. The curves were obtained by applying double potential steps; initially, a forward potential of 0.65 V and then a final reverse potential of 0.2 V. Fairly high glucose oxidation peak current was observed for 5CuO@TiO<sub>2</sub>-modified electrode. The order for peak currents observed for all of the modified electrodes is in good covenant with the electrocatalytic activity studied through cyclic voltammetric measurements and further validate all the electroanalytical findings. The interesting feature of the chronoamperograms is the constant current plateaus observed for all the modified electrodes when the double potential steps are applied and the electrodes were maintained at these steps for a period of 60 s each. This infers

**Table 2** Comparative performance of CuO-TiO<sub>2</sub> based electrodes for electrochemical glucose sensing

Electrode material	Linear range	Sensitivity ( $\mu\text{A mM}^{-1} \text{cm}^{-2}$ )	Detection limit	References
CuO/TiO <sub>2</sub> NT	Up to 2.0 mM	79.79	1.0 $\mu\text{M}$	[18]
NiO/CuO/Ti	0.1–1200 $\mu\text{M}$	1600	0.1 $\mu\text{M}$	[45]
Ni–Cu/TiO <sub>2</sub>	6.0 mM	719.9	30.0 $\mu\text{M}$	[46]
CuO/TiO <sub>2</sub>	10.0 $\mu\text{M}$ –2.0 mM	1321	390.0 nM	[19]
CuO/TiO <sub>2</sub>	6.8–12.5 mM	1416	3.4 $\mu\text{M}$	[47]
5CuO@TiO <sub>2</sub>	2.0–20.0 mM	7.15	235.0 $\mu\text{M}$	This work

**Fig. 8** Cyclic voltammogram for CuO@TiO<sub>2</sub>-modified electrode in 3.0 M KOH solution at a scan rate of 500 mV s<sup>-1</sup> (a). Graphical presentation of glucose electrooxidation mechanism on the modified electrode (b)

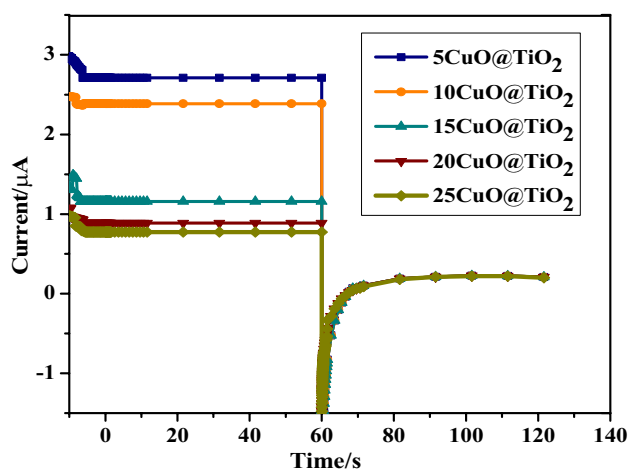
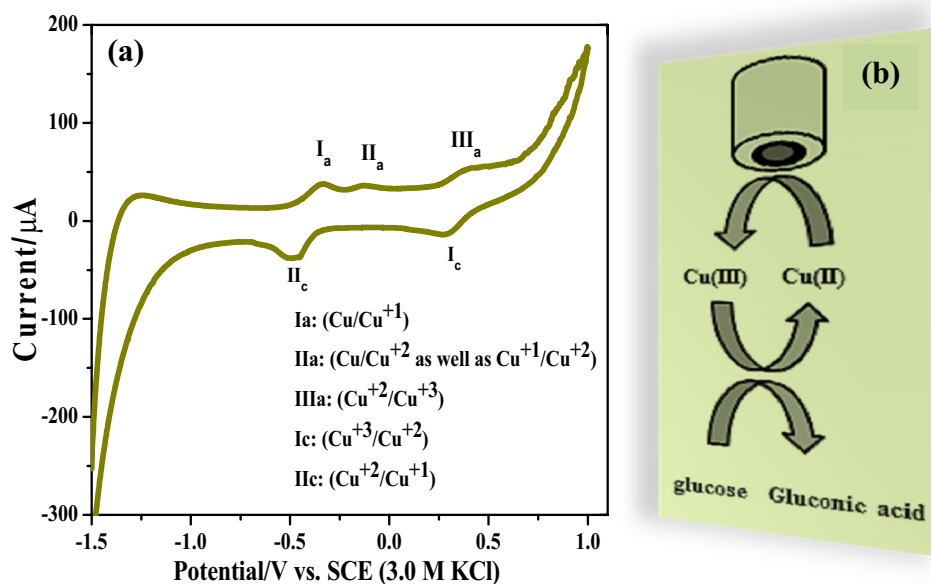


**Fig. 9** Chronoamperometric plots for 5-25CuO@TiO<sub>2</sub>-modified electrodes in 2.0 mM glucose concentration and 0.1 M KOH

toward electrochemical stability of the modified electrodes in the analyte of interest. Secondly, when the final potential is maintained the current values fall to a negligible value indicating irreversible nature of glucose electrooxidation on these modified electrodes resulting in constant negligible current values [51].

### Stability and reproducibility

The mechanical stability of 5CuO@TiO<sub>2</sub>-modified electrode was tested in terms of the electrooxidation of methanol in 0.1 M KOH at 100 mV s<sup>-1</sup> scan rate by cyclic voltammetry.

The reproducibility of voltammograms in 10 cycles was maintained, Fig. S7 (a). The reproducibility of the sensor was also determined by conducting five sequential amperometric measurements of 2.0 mM glucose with five 5CuO@TiO<sub>2</sub> electrodes prepared in a similar fashion. The anodic peak current response for 2.0 mM glucose is represented in the bar chart of Fig. S7 (b). Small disparity in the anodic current response was noted for the five identical electrodes. The average and relative standard deviation (RSD) of modified electrodes for these measurements were  $2.52 \pm 10.6\%$ .

Control experiments of bare GC electrode and TiO<sub>2</sub> without CuO loading were also performed in the same electrolyte (0.1 M KOH) at 100 mV s<sup>-1</sup> scan rate with and without methanol and glucose. The cyclic voltammograms presented in Fig. S8 indicate that electrooxidation of analytes was not observed on GC- and TiO<sub>2</sub>-modified GC electrodes. Comparative voltammograms of 5-25CuO@TiO<sub>2</sub> in 0.1 M KOH in absence of methanol and glucose are also presented for comparison.

### Conclusions

This study envisaged a simple fabrication method of CuO@TiO<sub>2</sub> mixed metal oxide catalysts with CuO in composition ranging from 5 to 25 wt%. All the prepared catalyst powders were subjected to physical and electrochemical characterization. The redox capabilities of 5-25CuO@TiO<sub>2</sub> mixed metal oxide catalysts were evaluated via cyclic voltammetry. Redox data were used to quantify the amount of CuO in each catalyst. Owing to the larger effective surface area, higher

electrical conductivity, and the lowest charge transfer resistance as revealed by CV and EIS studies, 5CuO@TiO<sub>2</sub> was proposed as a contender for further application studies on methanol and glucose. The Cu (II) to Cu (III) redox couple was evidently involved in the electrocatalytic oxidation process. Although all the prepared compositions manifested their potential role in the electrooxidation of methanol and glucose; however, 5CuO@TiO<sub>2</sub> responded with higher peak current profile for both the analytes. The proposed electrocatalysts also established their stability in alkaline media for both the analytes in terms of steady current response and reproducible current value. These electrocatalysts may prove to be the robust candidates for the future electroanalytical applications.

**Acknowledgements** The research work elucidated in this paper was carried out at laboratory provisions in Quaid-i-Azam University Islamabad. Authors greatly acknowledge NUST Islamabad for the SEM and EDX mapping facility. HEC Projects No. 1718 and 4768 are highly acknowledged for Gamry instrument.

## References

- O. Popovski, Electrocatalysts in the last 30 years—from precious metals to cheaper but sophisticated complex systems. *Bull. Chem. Technol. Maced.* **23**, 101–112 (2004)
- C. Qian, X. Guo, W. Zhang, H. Yang, Y. Qian, F. Xu, S. Qian, S. Lin, T. Fan, Co<sub>3</sub>O<sub>4</sub> nanoparticles on porous bio-carbon substrate as catalyst for oxygen reduction reaction. *Microporous Mesoporous Mater.* **277**, 45–51 (2019)
- X. Guo, C. Qian, R. Shi, W. Zhang, F. Xu, S. Qian, J. Zhang, H. Yang, A. Yuan, T. Fan, Biomorphic Co-N-C/CoOx composite derived from natural chloroplasts as efficient electrocatalyst for oxygen reduction reaction. *Small* **15**, 1804855 (2019)
- S. Thangavel, N. Raghavan, G. Venugopal, *Magnetically Separable Iron Oxide-Based Nanocomposite Photocatalytic Materials for Environmental Remediation, Photocatalytic Functional Materials for Environmental Remediation* (Wiley, 2019), pp. 243–265
- R. Raliya, T.S. Chadha, K. Haddad, P. Biswas, Perspective on nanoparticle technology for biomedical use. *Curr. Pharm. Des.* **22**, 2481–2490 (2016)
- S.Y. Tee, K.Y. Win, W.S. Teo, L.D. Koh, S. Liu, C.P. Teng, M.Y. Han, Recent progress in energy-driven water splitting. *Adv. Sci.* **4**, 1600337 (2017)
- Y. Chen, Y. Wu, C. Liu, L. Guo, J. Nie, Y. Chen, T. Qiu, Low-temperature conversion of ammonia to nitrogen in water with ozone over composite metal oxide catalyst. *J. Environ. Sci.* **66**, 265–273 (2018)
- L. Liu, P. Concepción, A. Corra, Modulating the catalytic behavior of non-noble metal nanoparticles by inter-particle interaction for chemoselective hydrogenation of nitroarenes into corresponding azoxy or azo compounds. *J. Catal.* **369**, 312–323 (2019)
- Z.D. Mahmoudabadi, E. Eslami, One-step synthesis of CuO/TiO<sub>2</sub> nanocomposite by atmospheric microplasma electrochemistry—Its application as photoanode in dye-sensitized solar cell. *J. Alloy. Compd.* **793**, 336–342 (2019)
- Q. Yang, M. Long, L. Tan, Y. Zhang, J. Ouyang, P. Liu, A. Tang, Helical TiO<sub>2</sub> nanotube arrays modified by Cu–Cu<sub>2</sub>O with ultrahigh sensitivity for the nonenzymatic electro-oxidation of glucose. *ACS Appl. Mater. Interfaces.* **7**, 12719–12730 (2015)
- A. Mujtaba, N.K. Janjua, Fabrication and electrocatalytic application of CuO@ Al<sub>2</sub>O<sub>3</sub> hybrids. *J. Electrochem. Soc.* **162**, H328–H337 (2015)
- A. Mujtaba, N.K. Janjua, Electrochemical sensing platform based on CuO@ CeO<sub>2</sub> hybrid oxides. *J. Electroanal. Chem.* **763**, 125–133 (2016)
- J.-H. Lee, J.-H. Kim, S.S. Kim, CuO–TiO<sub>2</sub> p–n core–shell nanowires: sensing mechanism and p/n sensing-type transition. *Appl. Surf. Sci.* **448**, 489–497 (2018)
- N.L. Reddy, S. Emin, V.D.S. Kumari, Muthukonda Venkatakrishnan, CuO quantum dots decorated TiO<sub>2</sub> nanocomposite photocatalyst for stable hydrogen generation. *Ind. Eng. Chem. Res.* **57**, 568–577 (2018)
- A.M. Kumar, A. Khan, R. Suleiman, M. Qamar, S. Saravanan, H. Dafalla, Bifunctional CuO/TiO<sub>2</sub> nanocomposite as nanofiller for improved corrosion resistance and antibacterial protection. *Prog. Org. Coat.* **114**, 9–18 (2018)
- B. Khodadadi, A.Y. Faal, A. Shahvarughi, Tilia platyphyllos extract assisted green synthesis of CuO/TiO<sub>2</sub> nanocomposite: application as a reusable catalyst for the reduction of organic dyes in water. *J. Appl. Chem. Res.* **13**, 51–65 (2019)
- S. Zhang, F. Chen, Y. Chi, Z. Dan, F. Qin, Non-enzymatic electrochemical glucose sensor based on Ti–Cu–O nanotubes prepared from TiCu amorphous alloy. *J. Nanosci. Nanotechnol.* **19**, 3825–3831 (2019)
- S. Luo, F. Su, C. Liu, J. Li, R. Liu, Y. Xiao, Y. Li, X. Liu, Q. Cai, A new method for fabricating a CuO/TiO<sub>2</sub> nanotube arrays electrode and its application as a sensitive nonenzymatic glucose sensor. *Talanta* **86**, 157–163 (2011)
- J. Chen, L. Xu, R. Xing, J. Song, H. Song, D. Liu, J. Zhou, Electrospun three-dimensional porous CuO/TiO<sub>2</sub> hierarchical nanocomposites electrode for nonenzymatic glucose biosensing. *Electrochem. Commun.* **20**, 75–78 (2012)
- M. Niu, W. Xu, S. Zhu, Y. Liang, Z. Cui, X. Yang, A. Inoue, Synthesis of nanoporous CuO/TiO<sub>2</sub>/Pd–NiO composite catalysts by chemical dealloying and their performance for methanol and ethanol electro-oxidation. *J. Power Sources* **362**, 10–19 (2017)
- A. Dicks, D.A.J. Rand, *Fuel Cell Systems Explained* (Wiley, London, 2018)
- R.-M. Yuan, H.-J. Li, X.-M. Yin, H.-Q. Wang, J.-H. Lu, L.-L. Zhang, Coral-like Cu–Co-mixed oxide for stable electro-properties of glucose determination. *Electrochim. Acta* **273**, 502–510 (2018)
- C. Chen, X.-L. Zhao, Z.-H. Li, Z.-G. Zhu, S.-H. Qian, A.J. Flewitt, Current and emerging technology for continuous glucose monitoring. *Sensors* **17**, 182 (2017)
- C. Canales, L. Gidi, G. Ramírez, Electrochemical activity of modified glassy carbon electrodes with covalent bonds towards molecular oxygen reduction. *Int. J. Electrochem. Sci.* **10**, 1684–1695 (2015)
- A. Shalan, M. Rashad, Y. Yu, M. Lira-Cantú, M. Abdel-Mottaleb, A facile low temperature synthesis of TiO<sub>2</sub> nanorods for high efficiency dye sensitized solar cells. *Appl. Phys. A* **110**, 111–122 (2013)
- S.M. Solyman, S.A. Hassan, S.A. Sadek, H.S. Abdel-Samad, Redox-initiated bulk polymerization of methyl methacrylate using a CuO/TiO<sub>2</sub> catalyst system. *Int. J. Polym. Mater.* **59**, 475–487 (2010)
- P.D. File, *Joint committee on powder diffraction standards* (ASTM, Philadelphia, PA, 1967), pp. 9–185
- D. Reyes-Coronado, G. Rodríguez-Gattorno, M. Espinosa-Pesqueira, C. Cab, R. De Coss, G. Oskam, Phase-pure TiO<sub>2</sub> nanoparticles: anatase, brookite and rutile. *Nanotechnology* **19**, 145605 (2008)
- J. Huang, S. Wang, Y. Zhao, X. Wang, S. Wang, S. Wu, S. Zhang, W. Huang, Synthesis and characterization of CuO/TiO<sub>2</sub> catalysts

- for low-temperature CO oxidation. *Catal. Commun.* **7**, 1029–1034 (2006)
30. Z. Liu, C. Zhou, Improved photocatalytic activity of nano CuO-incorporated TiO<sub>2</sub> granules prepared by spray drying. *Prog. Nat. Sci. Mater. Int.* **25**, 334–341 (2015)
  31. M. Liu, J. Chang, C. Yan, J. Bell, Comparative study of photocatalytic performance of titanium oxide spheres assembled by nanorods, nanoplates and nanosheets. *Int. J. Smart Nano Mater.* **3**, 72–80 (2012)
  32. S. Agarwala, M. Kevin, A. Wong, C. Peh, V. Thavasi, G. Ho, Mesophase ordering of TiO<sub>2</sub> film with high surface area and strong light harvesting for dye-sensitized solar cell. *ACS Appl. Mater. Interfaces.* **2**, 1844–1850 (2010)
  33. W.Z. Teo, A. Ambrosi, M. Pumera, Direct electrochemistry of copper oxide nanoparticles in alkaline media. *Electrochem. Commun.* **28**, 51–53 (2013)
  34. A. Ambrosi, M. Pumera, Redox-active nickel in carbon nanotubes and its direct determination. *Chem. Eur. J.* **18**, 3338–3344 (2012)
  35. A.J. Bard, L.R. Faulkner, *Fundamentals and Applications, Electrochemical Methods*, 2nd edn. (Wiley, New York, 2001)
  36. B. Derkus, E. Emregul, C. Yucesan, K.C. Emregul, Myelin basic protein immunosensor for multiple sclerosis detection based upon label-free electrochemical impedance spectroscopy. *Biosens. Bioelectron.* **46**, 53–60 (2013)
  37. S. Thiagarajan, M. Rajkumar, S.-M. Chen, Nano TiO<sub>2</sub>-PEDOT film for the simultaneous detection of ascorbic acid and diclofenac. *Int. J. Electrochem. Sci.* **7**, 2109–2122 (2012)
  38. S. Eloul, C. Batchelor-McAuley, R.G. Compton, Thin film-modified electrodes: a model for the charge transfer resistance in electrochemical impedance spectroscopy. *J. Solid State Electrochem.* **18**, 3239–3243 (2014)
  39. S.H. Aboutalebi, A.T. Chidembo, M. Salari, K. Konstantinov, D. Wexler, H.K. Liu, S.X. Dou, Comparison of GO, GO/MWCNTs composite and MWCNTs as potential electrode materials for supercapacitors. *Energy Environ. Sci.* **4**, 1855–1865 (2011)
  40. B.A. Boukamp, A linear Kronig-Kramers transform test for immitance data validation. *J. Electrochem. Soc.* **142**, 1885–1894 (1995)
  41. A. Nafady, Electrochemistry with the extremely weak coordinating anions: using of carboranes [H-CB11X6Y5] – (X = H, Cl, Br; Y = H or Me) as supporting electrolyte anions. *J. Electroanal. Chem.* **755**, 1–6 (2015)
  42. E. Biçer, P. Çetinkaya, Electrochemical behaviour of the antibiotic drug novobiocin sodium on a mercury electrode. *Croat. Chem. Acta* **82**, 573–582 (2009)
  43. V. Oncescu, D. Erickson, High volumetric power density, non-enzymatic, glucose fuel cells. *Sci. Rep.* **3**, 1226 (2013)
  44. Z.D. Gao, J. Guo, N.K. Shrestha, R. Hahn, Y.Y. Song, P. Schmuki, Nickel hydroxide nanoparticle activated semi-metallic TiO<sub>2</sub> nanotube arrays for non-enzymatic glucose sensing. *Chem. A Eur. J.* **19**, 15530–15534 (2013)
  45. R. Ding, J. Liu, J. Jiang, J. Zhu, X. Huang, Mixed Ni–Cu-oxide nanowire array on conductive substrate and its application as enzyme-free glucose sensor. *Anal. Methods* **4**, 4003–4008 (2012)
  46. A. Raziq, M. Tariq, R. Hussain, M.H. Mahmood, I. Ullah, J. Khan, M. Mohammad, Highly sensitive, non-enzymatic and precious metal free electrochemical glucose sensor based on Ni–Cu/TiO<sub>2</sub> modified glassy carbon electrode. *J. Serb. Chem. Soc.* **83**, 733–744 (2018)
  47. J. Stanley, R.J. Sree, T. Ramachandran, T. Babu, B.G. Nair, Vertically aligned TiO<sub>2</sub> nanotube arrays decorated with CuO mesoclusters for the nonenzymatic sensing of glucose. *J. Nanosci. Nanotechnol.* **17**, 2732–2739 (2017)
  48. X. Wang, C.-Y. Ge, K. Chen, Y.X. Zhang, An ultrasensitive non-enzymatic glucose sensors based on controlled petal-like CuO nanostructure. *Electrochim. Acta* **259**, 225–232 (2018)
  49. M.P. Sánchez, M. Barrera, S. González, R. Souto, R. Salvarezza, A. Arvia, Electrochemical behaviour of copper in aqueous moderate alkaline media, containing sodium carbonate and bicarbonate, and sodium perchlorate. *Electrochim. Acta* **35**, 1337–1343 (1990)
  50. M.M. El-Deeb, W.M. El Roubi, A. Abdelwahab, A.A. Farghali, Effect of pore geometry on the electrocatalytic performance of nickel cobaltite/carbon xerogel nanocomposite for methanol oxidation. *Electrochim. Acta* **259**, 77–85 (2018)
  51. A.A. Ensafi, B. Rezaei, Z. Mirahmadi-Zare, H. Karimi-Maleh, Highly selective and sensitive voltammetric sensor for captopril determination based on modified multiwall carbon nanotubes paste electrode. *J. Braz. Chem. Soc.* **22**, 1315–1322 (2011)